non-peer-reviewed EarthArXiv preprint

Weak phases production and heat generation controls fault friction during seismic slip

Hadrien Rattez*,[1] & Manolis Veveakis[1]

[1] *Civil and Environmental Engineering Department, Duke University*

The triggering and magnitude of earthquakes is determined by the friction evolution along faults. Experimental results have revealed a drastic decrease of the friction coefficient for velocities close to the maximum seismic one, independently of the material studied[1,2]. Due to the extreme loading conditions during seismic slip, many competing physical phenomena are occurring (like mineral decomposition [3], nanoparticle lubrication [1], melting [4] among others) that are typically thermal in origin[5] and are changing the nature of the material.

Here we show that a large set of experimental data for different rocks can be described by such thermally-activated mechanisms[6], combined with the production of weak phases. By taking under account the energy balance of all processes during fault movement, we present a framework that reconciles the data, and is capable of explaining the frictional behavior of faults, across the full range of slip velocities ($10^{-9} - 10$ m/s).

The similarity of microstructures observed in nature and in experiments suggests that energetic frameworks like the one presented could quantitatively link observations across the scales and provide deep, physics-based insight on the physical mechanisms driving seismic

slip.

The knowledge of the friction (shear strength) evolution along a pre-existing fault is of major importance, as it allows extracting many characteristics and features of seismic slip. In particular, the decrease of the friction with increasing velocity or displacement (a process called frictional weakening) determines the possible nucleation of earthquakes. If the weakening rate is larger than a critical value, this leads to the triggering of a dynamic slip at the origin of earthquakes[7]. In addition to nucleation, the evolution of the friction coefficient- and thus of the fault's shearing resistance- determines the arrest of the fault slip and governs the form and budget of energy dissipation during seismic slip[8]. The latter is essential as it determines the amount of energy produced at the fault, which is radiated on the surface through seismic waves and tremors.

During the last 20 years, a large set of experimental works has been devoted to reproducing the extreme conditions of a seismic slip. The development of high velocity shear apparatus allowed the research community to perform experiments at the maximum velocity reached during an earthquake event ($1 - 10$ m/s) and, thus, characterize the behaviour of a fault over the full range of possible slip rates [9]. A drastic decrease of the friction has been observed in most cases for velocities closed to the maximum slip velocity independently of the material considered[1], however the physical mechanisms accompanying this rapid weakening being different for each rock type. Following microstructural observations and measurements in the sheared samples, several thermally and mechanically activated weakening mechanisms were proposed to understand the experimental results at seismic slip rates[6]. The common feature of all these weakening mechanisms is phase

transformation -like mineral decomposition[3], nanoparticle lubrication[1], melting[4]- during which a change in the nature of the material takes place.

To describe the effect of such a weak phase on the frictional behaviour of a mixture of a strong/weak phase and constrain the influence of phase change on the mechanical behaviour, we consider first experiments looking at the effect of a weak phase on the frictional response of fault zones. The weak phases used for the tests are talc or saturated clay materials sheared at low velocities (lower than 10^{-5}m/s), so that the mechanisms described above are not triggered. The results are shown in Figure 1, where we may observe that the friction coefficient μ decreases as the weak phase fraction increases. This effect of the weak phase fraction can be captured using an exponential law $\mu = \mu_0 + \Delta\mu\ e^{-\alpha w}$, where μ_0 is the friction coefficient of the weak phase, $\Delta\mu = \mu_s - \mu_0$ is the difference of the friction coefficient of the strong and weak phases, w is the weak phase fraction and α a weakening coefficient ranging from 0.1 to 15 (see supplementary information). Note that such nonlinear weakening laws are also used in geomechanical engineering to describe the weathering of calcarenite[10,11].

The derived exponential decrease of the mechanical strength from the experimental data of Figure 1 is then included into a thermo-chemo mechanical model that accounts for the coupled mechanisms activated at higher velocity conditions (see Methods for the mathematical description of the model). In this model, the degradation or creation of a weak phase is induced by the energy input to the system and it is not present before shearing. This unifying approach aims at reconciling observations across a wide spectrum of materials and velocities. The extensive experimental

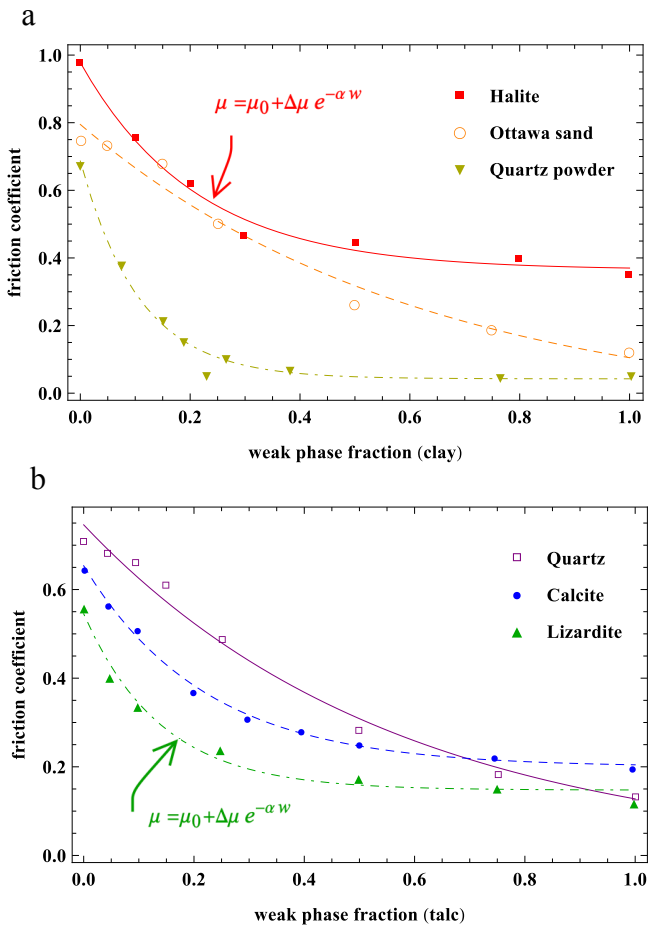

Figure 1: **Effect of the weak phase content on the steady state friction coefficient.** The friction of weak/strong phase binary mixtures is represented as function of the weak phase content in experiments carried out at subseismic sliding velocities and at constant normal stress using triaxial saw cut, double and simple direct shear and rotary shear configurations. **a**, results for clay as weak phase: red corresponds to a muscovite/halite mixture [12], orange to a crushed Ottawa sand/montmorillonite mixture [13] , dark yellow to a quartz powder/bentonite mixture [14]. **b**, results for talc as weak phase: purple corresponds to quartz as strong phase [15], blue to calcite [16] , green to Lizardite [15]. In **a-b**, the points represent the experimental data and the solid or dashed lines represent the interpolation using this exponential function.

data set used for the comparison corresponds to shear tests performed with rotary shear apparatus that allows to reach high displacements and therefore the steady state (see Figure 2). These experiments are realized on either gouge granular samples (usually 1mm thick[17]) sandwiched between two blocks or on bare rock samples[18]. In the latter, a gouge material is formed after only a few millimetres of displacement[2] with a thickness of 100 to 300 μm. The data are gathered based on the nature of the material sheared and the physical mechanisms that are inferred to operate during the experiments[1,19].

The constitutive law for the mechanical behaviour is applied to the gouge material, which accommodates all the deformation and is affected by the temperature, the weak phase fraction and the state of stress. The weak phase creation is modelled as an endothermic first order chemical transformation affecting the energy balance equation and respecting the mass balance. The geometry of the model chosen is larger of one or two orders of magnitude than the gouge in order to impose far field boundary conditions for the temperature and the extend of the phase transformation (see Figure 2). The steady states of this model can be determined using a continuation algorithm (see Methods), to test the hypothesis that the combination of thermally activated weakening and the creation of a weak phase may account for the observed steady state frictional response over many orders of magnitude of shear velocity.

The resulting steady state response of the model, in terms of friction and velocity, is depicted in Fig. 2. We can identify five distinct regimes of the system response to loading velocity: (I) **Static.** At low velocities, the material remains at static friction. Negligible temperature increase

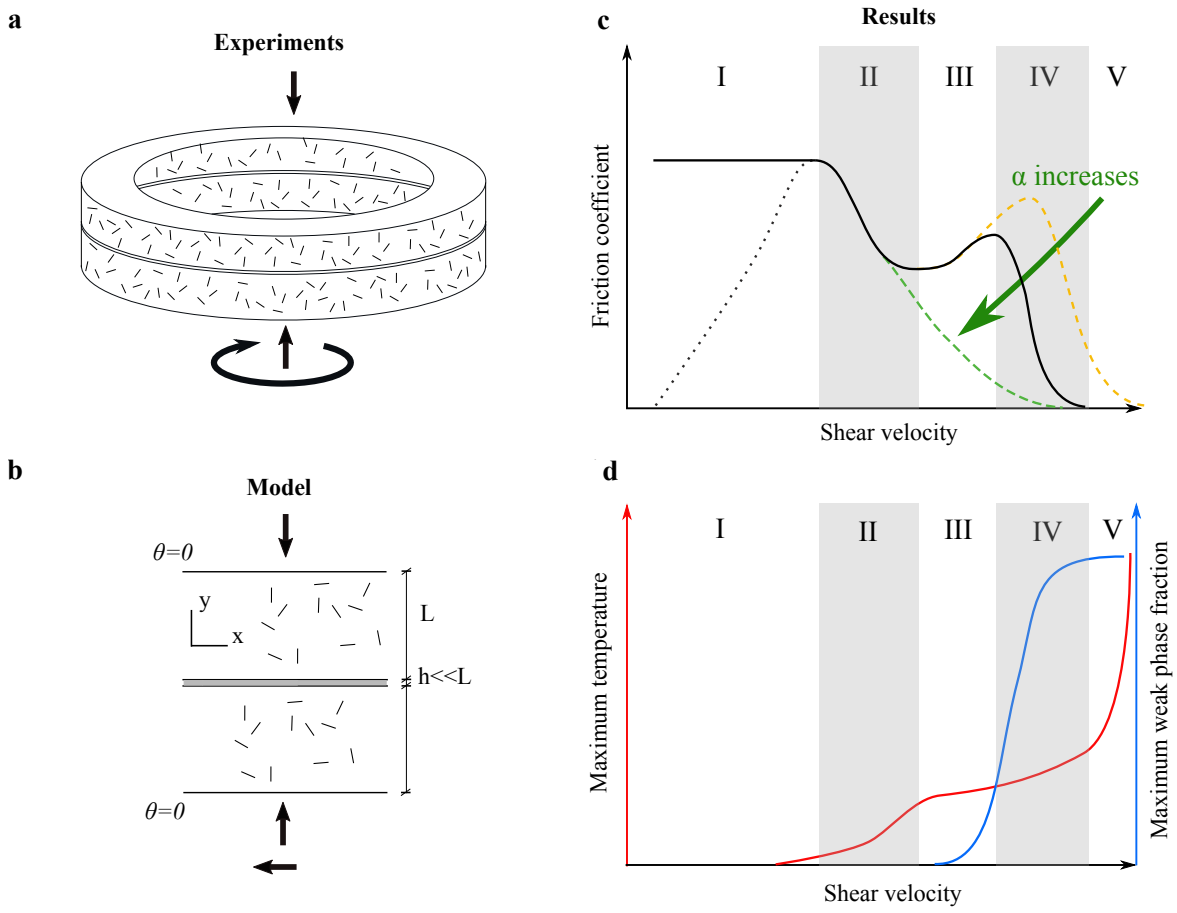

Figure 2: **a-b, Schematic view of the geometry of the high velocity rotary shear experiments and the model. c-d, Steady state of the thermo-chemo mechanical model.** Response of the mathematical system of equations (Eqs. 5-6 in Methods) at steady state. **c**, the steady state friction coefficient as a function of velocity, for varying weak phase sensitivity coefficient α. **d**, the steady-state temperature and weak phase content dependency on the velocity, plotted for the black line of **c**. The five regimes (I - V) that can be observed in the response of the friction coefficient are correlated with the temperature and weak phase production processes, as explained in the main text.

or weak phase production is observed. (II) **Thermo-mechanical weakening.** The temperature increase leads the friction coefficient to drop, in the absence of any weak phase production. (III) **Thermo-chemical stabilization.** With increasing velocity and temperature, small fractions of the weak phase are produced, absorbing the excess temperature and reducing the thermal softening effect on the friction coefficient. Depending on the value of the weakening coefficient, the friction coefficient can experience an intermediate increase. (IV) **Chemo-mechanical weakening.** Eventually, weak phase content will be produced until it reaches a critical value that will dominate the friction coefficient and lead the material to unconstrained weakening. (V) **Runaway instability.** Once the reactants are depleted ($w = 1$), the temperature is increasing uncontrollably and the friction coefficient drops towards zero.

After identifying the regimes of the steady frictional response of faults, the model is applied to experimental data. Figure 3 summarizes the results of the model for the steady state friction coefficient as a function of the velocity for six sets of materials[1,9,18–21]. The experimental data are a collection of several independent studies at different experimental conditions. As shown in the supplementary information, the normal stress shows no clear effect on the value of the friction coefficient reported here and for this reason it is not further investigated in this study. One of the interesting features of the model is the reproduction of strengthening observed experimentally at intermediate velocities (regime III in Figure 2) without supposing any additional hardening mechanism. For each material, the inferred phase transformation and the resulting weak product are highlighted. The model enables to capture accurately the observations and uses as input the material parameters listed in the supplementary information. Moreover, it enables us to retrieve

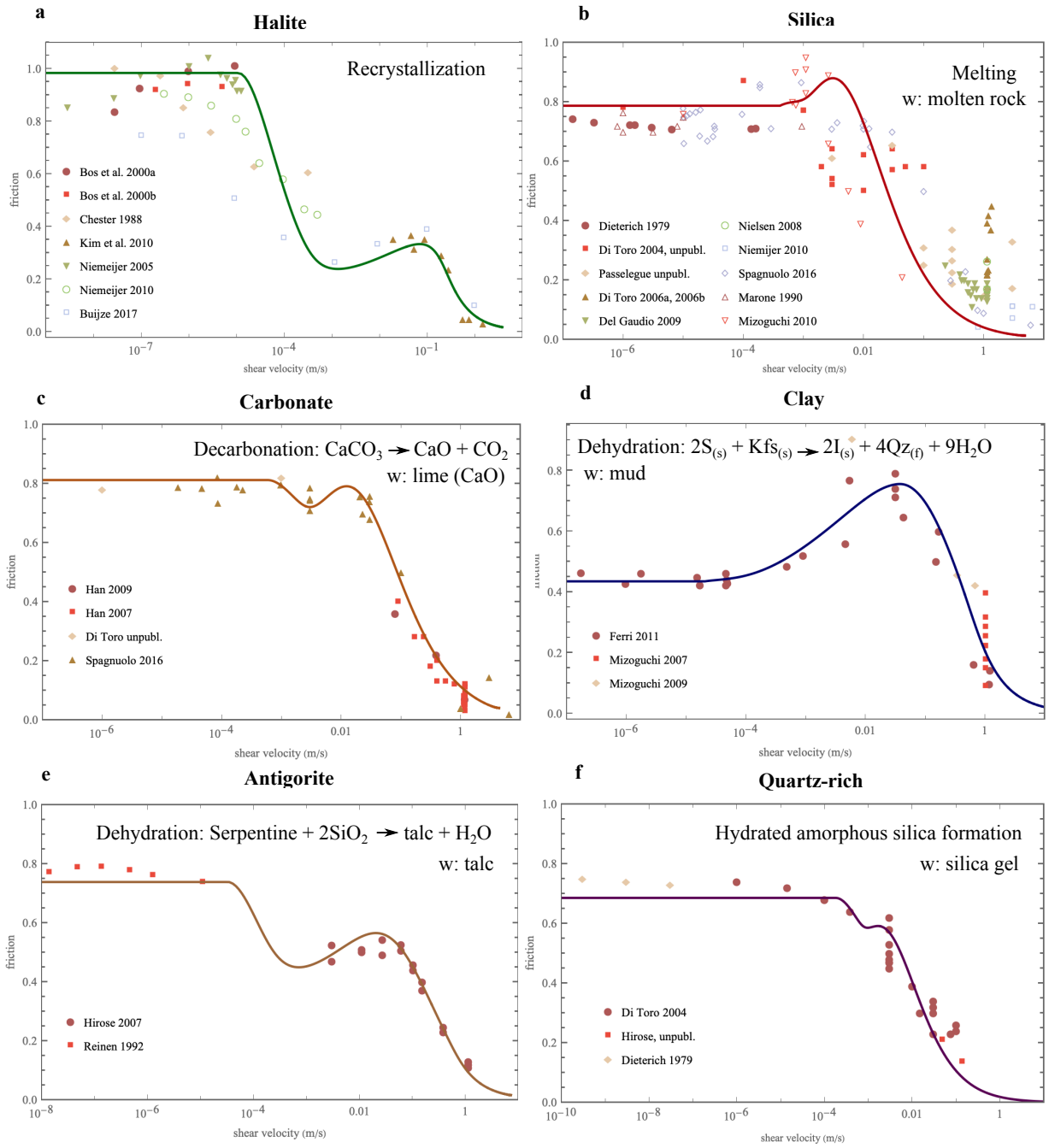

Figure 3: **Results of the model for different types of materials.** Application of the mathematical model (solid lines) to literature data (dots) of the friction coefficient as a function of the velocity. See the Methods for the mathematical description, Fig. 2 for the qualitative steady-state response and the supplementary information for the references of the experimental data. For each material, the phase transformation and the associated weak phase are indicated. **a**, for halite rock. The model reproduces the experimental behaviour with $\alpha = 0$. **b**, for silicate rocks ($\alpha = 7.5$). **c**, for carbonate rocks ($\alpha = 5.3$). **d**, for clay-rich rocks ($\alpha = 2$).

information for the parameters of the different processes such as the activation energies, together with an assessment of the temperature evolution. This can be used as a basis to compare with the microstructural observations of the samples after the experiments. Indeed, in Figure 4 we are summarizing the evolution of the Temperature and weak phase ratio w required to obtain the friction coefficient results of Figure 3. Based on these two figures, we can compile the processes underpinning the macroscopic response of the frictional resistance of the different materials.

The temperature predicted by the model when the weak phase begins to appear can be compared to the theoretical activation temperature of the phase transformation (decarbonation[22], melting[23], dehydration[24] or clay type transition[9]), when available. In all cases, the temperature of the model is lower than the theoretical one (e.g. 530° C against 720° C for carbonates) implying that the phase transition is triggered locally at the contact of the grains where the temperature can be higher than the bulk temperature. Moreover, these local phase changes are hard to detect even though essential for the mechanical behaviour. This also explains why the evidences of the phase transformations from specific sensors or microstructural observations (recrystallized halite grains[17], increase of CO_2[22] or humidity next to the tested sample[18], melted asperities[25] and white flakes due to silica gel[20]) are retrieved for higher velocities in experiments than predicted by the model. A notable case is halite, for which the weakening factor is $\alpha = 0$ implying that any weak phase generated during shear does not affect the friction coefficient. As the material undergoes recrystallisation[17] during shearing which is a phase transformation that produces the same mineral with different grain sizes. Despite not producing a weak phase directly though, recrystallisation affects the energy budget and, thus the temperature produced (Figure 4) and therefore the mechanical

behaviour of the gouge.

These results suggest that a thermally activated creep and the transformation of the material inside the fault zone may be the dominant mechanisms during seismic slip of dry rocks. In the case where pressurized fluids are present -a scenario difficult to study experimentally- the static friction response[9] and the transient behaviour through thermal pressurization[26,27] are likely to be affected. In that case a detailed comparison between phase transition and thermal pressurization needs to be carried, to assess the dominant mechanism of slip [28].

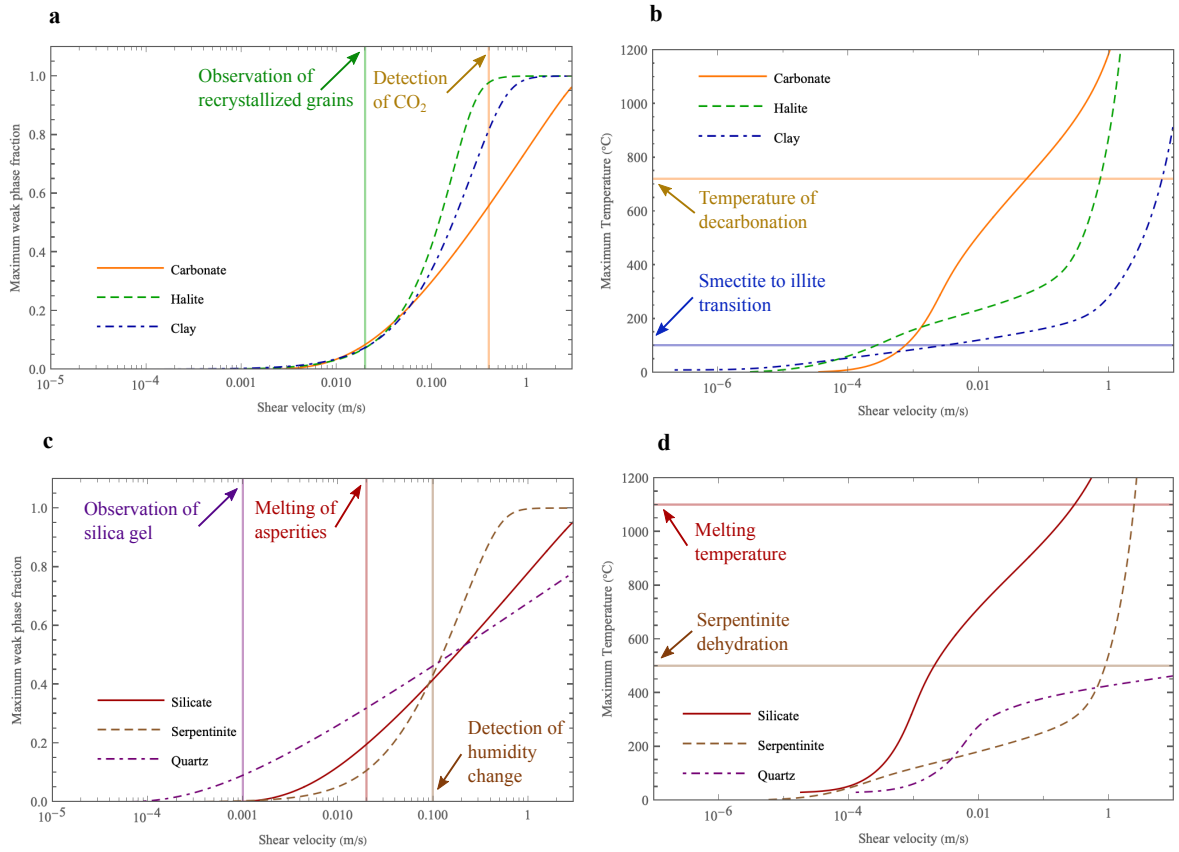

Figure 4: **Temperature and weak phase fraction evolution with the velocity for the experiments of Fig. 3.** **a** and **c**, weak phase fraction in the middle of the sample. Note that weak phase production has been approached as a first order chemical reaction, thus reaching its maximum value of one (100% weak phase present) when the reaction is depleted. **b** and **d**, maximum temperature in the middle of the sample.

Methods

Description of the Mathematical Model. When the shear velocity applied to a rock or a granular sample is increased, thermal effects tend to dominate the frictional response[5,20,29,30]. A critical velocity is required to activate this mechanism that is related to the processes at asperities or grain contacts[5]. In this paper, we focus on the response of the material for intermediate and high velocities where the thermal and chemical effect are important (other models have been developed for lower velocities and the nucleation of earthquakes[29,31]). Therefore, we consider here that for low velocities experiments the strength of the material is determined by the static friction of the materials in contact or the internal static friction of the granular assembly. For velocities larger than the critical one, the shear stress of the system is calculated by solving a thermo-chemo-mechanical model inside the deforming zone. The critical velocity is retrieved as a result from this model and can be approximated by an analytical solution (see supplementary information). Physically, it corresponds to the critical velocity for which thermal weakening becomes significant.

The mathematical model consists of solving the momentum, mass and energy balance equation at steady state, for an infinite sheared layer. The equations are briefly summarized here for easiness in reproducibility of the results[3].

The momentum balance equations are considered and we neglect the inertia terms[32]:

$$\sigma_{ij,j} = 0 \tag{1}$$

where σ_{ij} is the stress tensor. These equations lead in the case of one dimensional shear zone to a constant normal and shear stress in space inside the layer.

The constitutive law for the mechanical behaviour is a rigid elastic-viscoplastic law with the most generic form: an Arrhenius-power law dependency[3,33]. This law is only considered in a layer of thickness h, much smaller than the total thickness of the layer L (see Figure 2). This enables to describe the fact that after only a few millimetres of slip during the shear experiments on bare rocks, a thin layer of gouge materials forms. This layer composed of crushed grains from the initially rough surfaces has generally a thickness of 100-300 μm^2 and accommodates all the deformation. However, as the boundary conditions for the weak phase and the temperature are not well defined for this gouge layer, a domain of 1 cm is considered in order to apply Dirichlet boundary conditions for these fields.

$$\dot{\epsilon}^{vp} = \dot{\epsilon}^0 (\frac{\tau}{\tau_y})^m e^{-Q/RT} \tag{2}$$

where $\dot{\epsilon}^0$ is a reference strain rate, m is the exponent of the power law, τ is the shear stress,τ_y is the yield stress, Q is an activation enthalpy for the microscopic mechanism inducing a nonlinear behaviour, R is the perfect gas constant and T is the temperature. This law allows to include more physics into the hardening evolution as in the theory of plasticity for metals[33]. The Arrhenius dependency of the flow law enables to introduce multi-physical couplings such as the effect of heat generation on the frictional strength or more generally interface phenomena between the solid skeleton and the pores[34,35].

The effect of the non-mechanical state variables on the mechanical behaviour of the system can be expressed as a single scalar function called the weathering index[11], X_d. The strength of the material depends on both the plastic strain and this weathering index. It is assumed that the two

effects are uncoupled[10,11] and a multiplicative structure of the yield stress is postulated:

$$\tau_y = T_y(\epsilon^p)T_y(X_d) \tag{3}$$

In our case, we do not consider any purely mechanical hardening law, so that the function $T_y(\epsilon^p)$ is constant. Moreover, X_d is considered to be a weak phase volume fraction. As shown in Figure 1, the presence of a weak phase induces an exponential decrease of the frictional strength along with the weak phase fraction. Assuming negligible shear strength for the weak phase, the final form of the constitutive law is therefore:

$$\dot{\epsilon}^{vp} = \dot{\epsilon}^0(\frac{\tau}{\tau_0})^m e^{-Q/RT} e^{\alpha\ m\ w} \tag{4}$$

where τ_0 is the yield strength of the strong phase and α is the weak phase sensitivity coefficient.

For a material consisting of two species: a weak and a strong phase, occupying volumes V_w and V_s respectively, we may define the volume ratio $w = \frac{V_w}{V_w+V_s}$. Inside a one dimensional shear zone yield a system of two equations[3,36] obtained from the mass balance of the weak phase fraction and the energy balance equations:

$$\frac{\partial T}{\partial t} = c_{th}\frac{\partial^2 T}{\partial y^2} + F(y)\frac{\tau\dot{\epsilon}^{vp}}{\rho C} - \frac{\Delta H\ r_F}{\rho C} \tag{5}$$

$$\frac{\partial \rho_1}{\partial t} + \frac{\partial J_w}{\partial y} = r_F \tag{6}$$

where T is the temperature, c_{th} the thermal diffusivity, ρC the heat capacity of the mixture considered constant here, J_w the diffusion flux of the weak phase, ΔH the enthalpy of the phase change reaction considered endothermic, r_F the reaction rate and $\rho_1 = \rho_w w$. $F(y)$ is a function which value is 1 for $y \in [-h/2, h/2]$ and 0 otherwise. The reaction rate is expressed as first order

chemical reaction with an Arrhenius law.

$$r_F = (1-w)\frac{\rho_s}{M_s} k_F e^{-Q_c/RT} \tag{7}$$

where ρ_s and M_s are the density and molar mass of the strong phase. k_F and Q_c are the preexponential factor and activation energy of the chemical reaction. Using Equations 4, 7, considering a Fick's law for the diffusion flux (defining a diffusivity c_w) and the steady state of Equations 5 and 6, we obtain a system of two differential equations in space. This system is written in a dimensionless form for the purpose of reducing the number of parameters to study and to enable a clearer understanding of the main features of the system:

$$\frac{\partial^2 \theta}{\partial \bar{y}^2} + F(\bar{y}) Gr\, e^{\frac{Ar\ \theta}{1+\theta}} e^{\alpha\ m\ w} - Da(1-w)\, e^{\frac{Arc\ \theta}{1+\theta}} = 0 \tag{8}$$

$$\frac{\partial w}{\partial \bar{y}^2} + \mu\, Da(1-w)\, e^{\frac{Arc\ \theta}{1+\theta}} = 0 \tag{9}$$

where, θ is the dimensionless temperature. Gr, Da, Ar and Arc are called the Gruntfest, Damköhler, Arrhenius and chemical Arrhenius numbers respectively. They are defined by:

$$Ar = \frac{Q}{R\, T_0}, \qquad Arc = \frac{Qc}{R\, T_0} \tag{10}$$

$$Gr = \frac{\tau_0\ \dot{\epsilon}_0\ L^2}{\rho C c_{th}\ T_0} \left(\frac{\tau}{\tau_0}\right)^{m+1} e^{-Ar} \tag{11}$$

$$Da = \frac{\Delta H\ k_F\ \rho_s\ L^2}{\rho C M_s c_{th}\ T_0} e^{-Arc} \tag{12}$$

$$\mu = \frac{\rho C c_{th}\ T_0 M_w}{\Delta H\ \rho_w\ c_w} \tag{13}$$

Numerical Bifurcation of the Steady State friction coefficient. The solutions of this nonlinear system of differential equations are approximated numerically using pseudospectral methods. The temperature and weak phase fraction fields are interpolated in space using Chebyshev polynomials

of the first kind:

$$\theta(\bar{y}) = \sum_{i=1}^{N} a_i \, (\phi_{2i}(\bar{y}) - 1) \tag{14}$$

$$w(\bar{y}) = \sum_{i=1}^{N} b_i \, (\phi_{2i}(\bar{y}) - 1) \tag{15}$$

where ϕ_{2i} are the Chebyshev polynomials of degree $2i$. Note that only the even degree Chebyshev polynomials are kept here as the solution is symmetric about the origin. Moreover, a basis recombination is used by considering interpolation functions of the form $\psi_{2i}(y) = \phi_{2i}(y) - 1$, allowing to enforce a zero Dirichlet boundary conditions implicitly[38]. N is the number of polynomials used to simulate the solutions. A convergence analysis has been conducted in each case to verify that N is high enough to have a negligible error on the solution. a_i and b_i are the interpolation coefficients for the temperature and the weak phase fraction respectively. The interpolation points used for the resolution are the Gauss-Lobato points defined by:

$$x_j = \cos(\frac{(2j-1)\pi}{4N}), \qquad j = 1, ..., N \tag{16}$$

The nonlinear system of algebraic equations obtained is solved using the Newton-Raphson method. In order to capture all the steady state solutions of the system for the different values of the stress, a continuation pseudo-arclength algorithm is used. The continuation parameter chosen is the Gruntfest number[3].

1. Di Toro, G. *et al.* Fault lubrication during earthquakes. *Nature* **471**, 494–498 (2011). URL http://www.nature.com/doifinder/10.1038/nature09838.

2. Reches, Z. & Lockner, D. A. Fault weakening and earthquake instability by powder lubrication. *Nature* **467**, 452–455 (2010). URL http://www.nature.com/doifinder/10.1038/nature09348.

3. Veveakis, E. *et al.* Chemical reaction capping of thermal instabilities during shear of frictional faults. *Journal of the Mechanics and Physics of Solids* **58**, 1175–1194 (2010). URL http://www.sciencedirect.com/science/article/pii/S0022509610001262.

4. Di Toro, G., Pennacchioni, G. & Teza, G. Can pseudotachylytes be used to infer earthquake source parameters? An example of limitations in the study of exhumed faults. *Tectonophysics* **402**, 3–20 (2005).

5. Rice, J. R. Heating and weakening of faults during earthquake slip. *Journal of Geophysical Research: Solid Earth* **111** (2006).

6. Niemeijer, A. *et al.* Inferring earthquake physics and chemistry using an integrated field and laboratory approach. *Journal of Structural Geology* **39**, 2–36 (2012).

7. Scholz, C. H. *The mechanics of earthquakes and faulting* (Cambridge, 2002), second edi edn.

8. Kanamori, H. & Brodsky, E. E. The physics of earthquakes. *Reports on Progress in Physics* **67**, 1429–1496 (2004).

9. Ferri, F. *et al.* Low- to high-velocity frictional properties of the clay-rich gouges from the slipping zone of the 1963 Vaiont slide, northern Italy. *Journal of Geophysical Research: Solid Earth* **116**, 1–17 (2011).

10. Ciantia, M. O. & Hueckel, T. Weathering of submerged stressed calcarenites: chemo-mechanical coupling mechanisms. *Géotechnique* **63**, 768–785 (2013).

11. Nova, R., Castellanza, R. & Tamagnini, C. A constitutive model for bonded geomaterials subject to mechanical and/or chemical degradation. *International Journal for Numerical and Analytical Methods in Geomechanics* **27**, 705–732 (2003). URL http://doi.wiley.com/10.1002/nag.294.

12. Niemeijer, A. R. & Spiers, C. J. Influence of phyllosilicates on fault strength in the brittle-ductile transition: insights from rock analogue experiments. *Geological Society, London, Special Publications* **245**, 303–327 (2005). URL http://books.google.com/books?hl=en&lr=&id=1oMGwL8ExU0C&oi=fnd&pg=PA303&

13. Tembe, S., Lockner, D. A. & Wong, T. F. Effect of clay content and mineralogy on frictional sliding behavior of simulated gouges: Binary and ternary mixtures of quartz, illite, and montmorillonite. *Journal of Geophysical Research: Solid Earth* **115**, 1–22 (2010).

14. Oohashi, K., Hirose, T., Takahashi, M. & Tanikawa, W. Dynamic weakening of smectite-bearing faults at intermediate velocities: Implications for subduction zone earthquakes. *Journal of Geophysical Research : Solid Earth* **120**, 1572–1586 (2015).

15. Moore, D. E. & Lockner, D. A. Frictional strengths of talc-serpentine and talc-quartz mixtures. *Journal of Geophysical Research: Solid Earth* **116**, 1–17 (2011).

16. Giorgetti, C., Carpenter, B. M. & Collettini, C. Frictional behavior of talc-calcite mixtures. *Journal of Geophysical Research: Solid Earth* **120**, 6614–6633 (2015).

17. Buijze, L., Niemeijer, A. R., Han, R., Shimamoto, T. & Spiers, C. J. Friction properties and deformation mechanisms of halite(-mica) gouges from low to high sliding velocities. *Earth and Planetary Science Letters* **458**, 107–119 (2017). URL http://dx.doi.org/10.1016/j.epsl.2016.09.059.

18. Hirose, T. & Bystricky, M. Extreme dynamic weakening of faults during dehydration by coseismic shear heating. *Geophysical Research Letters* **34**, 10–14 (2007).

19. Spagnuolo, E., Nielsen, S., Violay, M. & Di Toro, G. An empirically based steady state friction law and implications for fault stability. *Geophysical Research Letters* **43**, 3263–3271 (2016).

20. Di Toro, G., Goldsby, D. L. & Tullis, T. E. Friction falls towards zero in quartz rock as slip velocity approaches seismic rates. *Nature* **427**, 436–439 (2004).

21. Hirose, T., Mizoguchi, K. & Shimamoto, T. Wear processes in rocks at slow to high slip rates. *Journal of Structural Geology* **38**, 102–116 (2012). URL http://dx.doi.org/10.1016/j.jsg.2011.12.007.

22. Han, R., Shimamoto, T., Hirose, T., Ree, J. H. & Ando, J. Ultralow friction of carbonate faults caused by thermal decomposition. *Science* **316**, 878–881 (2007).

23. Hirose, T. & Shimamoto, T. Growth of molten zone as a mechanism of slip weakening of simulated faults in gabbro during frictional melting. *Journal of Geophysical Research: Solid Earth* **110**, 1–18 (2005).

24. Poulet, T., Veveakis, M., Regenauer-Lieb, K. & Yuen, D. A. Thermo-poro-mechanics of chemically active creeping faults : 3 . The role of serpentinite in episodic tremor and slip sequences , and transition to chaos. *Journal of Geophysical Research* **119**, 4606–4625 (2014).

25. Goldsby, D. L. & Tullis, T. E. Flash Heating Leads to Low Frictional Earthquake Slip Rates. *Science* **334**, 216–218 (2011).

26. Viesca, R. C. & Garagash, D. I. Ubiquitous weakening of faults due to thermal pressurization. *Nature Geoscience* **8**, 875–879 (2015). URL http://www.nature.com/doifinder/10.1038/ngeo2554.

27. Rattez, H., Stefanou, I., Sulem, J., Veveakis, M. & Poulet, T. The importance of Thermo-Hydro-Mechanical couplings and microstructure to strain localization in 3D continua with application to seismic faults . Part II : Numerical implementation and post-bifurcation analysis. *Journal of the Mechanics and Physics of Solids* **115**, 1–29 (2018).

28. Veveakis, M., Poulet, T. & Alevizos, S. Thermo-poro-mechanics of chemically active creeping faults: 2. Transient considerations. *Journal of Geophysical Research: Solid Earth* n/a–n/a (2014).

29. Chen, J., Niemeijer, A. R. & Spiers, C. J. Microphysically Derived Expressions for Rate-and-State Friction Parameters, a, b, and Dc. *Journal of Geophysical Research: Solid Earth* **122**, 9627–9657 (2017).

30. Proctor, B. P. *et al.* Dynamic weakening of serpentinite gouges and bare surfaces at seismic slip rates. *Journal of Geophysical Research : Solid Earth* **119**, 8107–8131 (2014).

287 31. Aharonov, E. & Scholz, C. H. A Physics-Based Rock Friction Constitutive Law: Steady State
288 Friction. *Journal of Geophysical Research: Solid Earth* **123**, 1591–1614 (2018).

289 32. Rice, J. R., Rudnicki, J. W. & Platt, J. D. Stability and localization of rapid shear in fluid-
290 saturated fault gouge : 1 . Linearized stability analysis. *Journal of Geophysical Research*
291 1–23 (2014).

292 33. Frost, H. J. & Ashby, M. F. *Deformation-Mechanism Maps, The Plasticity and Creep of Metals*
293 *and Ceramics* (Pergamon Press, 1982).

294 34. Einav, I. The unification of hypo-plastic and elasto-plastic theories. *In-*
295 *ternational Journal of Solids and Structures* **49**, 1305–1315 (2012). URL
296 http://dx.doi.org/10.1016/j.ijsolstr.2012.02.003.

297 35. Veveakis, E. & Regenauer-Lieb, K. Cnoidal waves in solids. *Jour-*
298 *nal of the Mechanics and Physics of Solids* **78**, 231–248 (2015). URL
299 http://dx.doi.org/10.1016/j.jmps.2015.02.010.

300 36. Sulem, J. & Famin, V. Thermal decomposition of carbonates in fault zones: Slip-weakening
301 and temperature-limiting effects. *Journal of Geophysical Research* **114**, 1–14 (2009).

302 37. Green II, H. W., Shi, F., Bozhilov, K., Xia, G. & Reches, Z. Phase transformation and nano-
303 metric flow cause extreme weakening during fault slip. *Nature Geoscience* **8**, 484–489 (2015).

304 38. Boyd, J. P. *Chebyshev and Fourier Spectral Methods: second edition* (2000).

305 **Acknowledgements** This work was supported by the Southern California Earthquake Center (SCEC),

306 award number 118062196. SCEC is funded by NSF Cooperative Agreement EAR-1033462 and USGS
307 Cooperative Agreement G12AC20038.

308 **Author contributions** MV and HR contributed to the development of the model. HR contributed to the
309 numerical implementation of the model and the comparison with experimental data. HR and MV contributed
310 to the writing of the paper.

311 **Competing Interests** The authors declare that they have no competing financial interests.

312 **Correspondence** Correspondence and requests for materials should be addressed to Hadrien Rattez. (email:
313 hadrien.rattez@duke.edu).